Experimental Investigation of the Relationship between Strain and Scalar Dissipation in Gas-Phase Turbulent Jets

P.S. Kothnur* and N.T. Clemens‡

Center for Aeromechanics Research
Department of Aerospace Engineering and Engineering Mechanics
The University of Texas at Austin
Austin, TX 78712-1085

Abstract

A study is described that is aimed at investigating the strain/scalar dissipation layer relationship in unity Schmidt number turbulent flows. This analysis makes use of simultaneous PIV/acetone PLIF data that were acquired in a previous study of turbulent planar nonreacting jets. In particular, we seek to investigate the extent to which the measured strain field can be used to predict the structure of the measured scalar dissipation layers. A comparison of the strain/dissipation layer relationship with the theoretical, 1-D opposed flow solution corresponding to a steady uniform strain field was made, and the results suggest that it is not possible to correctly predict dissipative layer length scales based on this simplified theory. Several different reasons for the lack of agreement with the simple theory are considered, but we believe that unsteady effects are the dominant reason. To investigate unsteady effects, the unsteady scalar transport equation was solved numerically, where a uniform strain field was imposed that varied sinusoidally in time. The results of this simplified model appear to capture the qualitative trends seen in the measured data.

Introduction

Theoretical studies of turbulent non-premixed flames have suggested that the structure of the reaction zone is strongly coupled to the underlying strain rate field through the influence of fluctuating strain on the scalar dissipation rate[1,2]. However, it is very difficult to explore the strain/dissipation relationship experimentally in turbulent flames owing to the difficulty of measuring the conserved scalar field in a reacting flow. For this reason, most of what is known of this relationship is inferred from non-reacting high Schmidt number turbulent mixing studies[3] or from direct numerical simulations of turbulence[4,5] (the Schmidt number is defined as $Sc = \nu/D$, where ν is the kinematic viscosity and D the mass diffusivity). These studies show that for both $Sc \approx 1$ and $Sc \gg 1$ fluids, the scalar dissipation field is composed of sheet-like structures, which appear to be oriented orthogonal to the direction of the most compressive principal strain rate. The scalar length scales are set by the competition between the thinning effect of compressive strain and the thickening effect of diffusion.[6] For $Sc \gg 1$, the scalar gradients are much thinner than the velocity gradients, thus scalar dissipation structures are generated by the application of a nearly uniform strain field.[3,6]

To date, there are few measurements of the relationship between the strain and scalar fields in unity Schmidt number turbulent flows. Theory suggests, however, that the inner-scale strain will be correlated over a length scale of the same order as the scalar gradient length scale. In this case, we would not expect the strain to be uniform over the scalar gradient length scales, and therefore both the strain field and the dissipation field may exhibit a more complex structure than at high Schmidt number. Therefore, the focus of the present study is to investigate the fundamental relationship between strain and scalar dissipation by analyzing simultaneous scalar/velocity data that were acquired in a previous study of non-reacting turbulent planar jets.[7,8]

---

* Graduate Research Assistant
† Associate Professor, Senior Member AIAA

A dissipation "sheet" (equivalently, "layer") occurs when the strain is compressive in one direction and extensive in the orthogonal directions,[6] as shown in Figure 1. The dissipative length scale is set by the competition between the thinning effect of the local principal compressive strain rate, S_{xx} and the thickening effect due to molecular diffusion.

The concentration ζ of a dynamically passive scalar evolves according to the scalar transport equation,

$$\left[\frac{\partial}{\partial t} + \mathbf{u}\cdot\nabla - \frac{1}{ReSc}\nabla^2\right]\zeta(n,t) = 0 \qquad (1)$$

In turbulent flows, the local strain rate is a function of both space and time. However, if it is assumed that this strain field is uniform, then the conserved scalar concentration along the compressive strain axis satisfies the 1D, unsteady scalar transport equation

$$\frac{\partial\zeta}{\partial t} + (-S_{xx}n)\frac{\partial\zeta}{\partial x} - D\frac{\partial^2\zeta}{\partial x^2} = 0 \qquad (2)$$

where x is the coordinate normal to the sheet. This equation has the steady state solution[6],

$$\frac{\zeta(x,t)-\zeta^-}{\zeta^+-\zeta^-} = \frac{1}{2}\left(1+erf\left(\frac{x}{\lambda_D}\right)\right) \qquad (3)$$

where ζ^+ and ζ^- are the scalar values at x = +∞ and x = -∞, respectively, and λ_D is the strain-limited mass diffusion scale, defined as,

$$\lambda_D = \sqrt{\frac{2D}{S_{xx}}} \qquad (4)$$

The steady state scalar concentration and dissipation profile are shown in Figure 2. As was done in Ref. 6, we use a somewhat different definition of λ_D, which also scales as $\sqrt{D/S_{xx}}$, but which is easier to compute from experimental data. Specifically, we use the full width at 20% of the maximum dissipation. In this case, we can define a non-dimensional quantity that has a constant value per the relation,

$$\alpha = \left[\frac{1}{\lambda_D}\right]_{20\%}\sqrt{\frac{D}{S_{xx}}} \approx 0.4 \qquad (5)$$

or equivalently,

$$\lambda_D \approx 2.5\sqrt{\frac{D}{S_{xx}}} \qquad (6)$$

One of the principal aims of this study is to determine how reasonably Equation (6), using measured values of S_{xx}, predicts the observed scalar dissipation layer length scales, λ_D, in a turbulent flow.

Experimental conditions

The data used in this study were acquired in a previous experimental study by Rehm.[7,8] The measurements were made in a planar co-flowing turbulent jet at local Reynolds numbers ranging from 1000 to about 6000. (The Reynolds number was based on the local centerline excess velocity, $\Delta U_c = U_0 - U_\infty$, and the full-width-at-half-maximum of the velocity profiles, $\delta_{50\%}$). The planar jet exit had a width of 1 mm with an aspect ratio of 150:1, and was surrounded by a slow co-flow of air (velocity approximately 0.1 m/s). The jet fluid consisted of air diluted with 30% acetone vapor (by volume). The primary measurements made consisted of simultaneous acetone planar laser-induced fluorescence (PLIF) and particle image velocimetry (PIV). The acetone PLIF provides the conserved scalar field and PIV provides the two-component velocity field within a plane. The field of view for both the PIV and PLIF images was 33 mm × 33mm. The flow conditions are shown in Table 1.

Table 1: Run conditions.

Case	Centerline velocity(U_c) (m/s)	$\delta_{50\%}$ (mm)	Approximate Local Reynolds number(Re_δ)
1	0.94	16.1	1000
2	0.59	31.5	2590
3	0.73	31.5	1500
4	2.52	25	4200
5	3.01	25.6	5140
6	2.15	42.8	6130

Data analysis

The raw PLIF images were post-processed to correct for non-uniform laser sheet illumination and background reflections/scattering. The resulting images were then low-pass filtered, and rescaled. Figure 3a

shows a sample PLIF image, a part of an ensemble of 50 images for each run. The 2-D scalar dissipation rate field is then computed over the entire image, as shown in Figure 3b.

Processing of the PIV data involves use of a hybrid PIV/particle tracking velocimetry technique[10] to compute velocity. The technique involves using a conventional cross-correlation for a predictor step followed by local cross-correlations of individual particles to obtain particle pair displacements. Figure 3c shows the validated vector field obtained from conventional PIV processing with a 32×32 window. These vectors are then used as an initial estimate in the particle tracking calculation. The particle tracking technique yields one velocity vector for each particle pair detected in the PIV images. Post processing on the PTV vector maps involves validation with the original PIV vector data and other standard validation techniques. The resulting vector field is then interpolated over a uniform grid, the interpolation grid size chosen based on the density of vectors in the PTV vector field. Typically, the particle tracking calculation detected enough particle pairs to allow us to interpolate the vectors onto a 122×122 grid, which corresponds to a resolution of 0.25 mm in the vector field. Figure 3d shows the vectors from the enhanced resolution computation over the region in space marked in Figure 3c.

Since our PIV data provide only 2-D velocity information, only the inplane components (s_{xx}, s_{xy}, s_{yx}, s_{yy}) of the strain rate tensor, $\boldsymbol{S}=(1/2)(\partial u_i/\partial x_j+\partial u_j/\partial x_i)$, can be computed. The 2-D information is sufficient to calculate the correct in-plane principal strains if we restrict the analysis to only those regions where the *z*-axis (the axis orthogonal to the laser sheet) is already a principal axis, or where the flow is locally 2-D. Given that the flow is turbulent, the second condition is highly unlikely. However, following the approach of Rehm and Clemens,[9] we argue that, if layers with high dissipation are considered, then it is likely that the laser sheet was oriented approximately orthogonal to the dissipation layer, in which case the *z*-axis is a principal axis. In this case, the *z*-direction shear components of the strain rate tensor are very small, and the two-component strain data can be related to the correct principal strains.

In view of the above assumption, only layers with high dissipation were considered. The dissipation field was first binarized with a suitable threshold (typically 60 % of the maximum dissipation in the image), resulting in a binary image with high dissipation regions set to one, and low dissipation regions set to zero. The resulting image was then processed by binary morphological operations to form a "skeleton" image of the layers. Connectivity conditions are then imposed, and a binary dissipation layer-centerline image was constructed. The layers were further validated by requiring layers to be "isolated". An "isolated" layer was defined as one in which the dissipation falls, on either side, to 20% of the maximum dissipation across the layer before increasing again[6]. Once a layer centerline was identified, data were extracted along a line orthogonal to the layer. The data extracted include the scalar, the scalar dissipation and the principal compressive strain rate.

The resolution of the PLIF imaging system, based on the size of a pixel in the flow field, is approximately 70 μm. However, subsequent post-processing such as filtering and smoothing results in significant loss of resolution, and the effective resolution of the acetone PLIF images is about 300 μm. Furthermore, although the PIV resolution is about 250 μm, the derivative are computed using values from several proximate points, and thus the resolution for the derived quantities is about 500 μm.

The expected strain-limited mass diffusion length scale is given by

$$\lambda_D = \Lambda \delta_{5\%}\, \mathrm{Re}_{\delta_{5\%}}^{-3/4}\, Sc^{-1/2} \qquad (7)$$

where the Reynolds number and the outer scale $\delta_{5\%}$ are based on the full width at the 5% jet velocity point. From studies of co-flowing jets, Buch and Dahm[6] measured Λ to be 11.2. The value of Λ based on $\delta_{50\%}$ and $\mathrm{Re}_{\delta 50\%}$ is about 14. Using this value of Λ, the value of λ_D is estimated to range from 1.5 ~ 4 mm, and the viscous length scale, λ_v, given by $\lambda_v = \lambda_D(\mathrm{Sc})^{1/2}$, is of the same order, since $Sc \approx 1$. Therefore, in all cases the strain-limited diffusion scales are resolved.

Results and discussion

The data corresponding to the five Reynolds numbers shown in Table 1 were analyzed. A data set consisted of an ensemble of 50 simultaneous PIV/PLIF images, and two data sets for each case were considered in the analysis. Typically, about 500 layers were identified for each case.

Figures 3a through 3f shows sample results for $\mathrm{Re}_{\delta 50\%}$=4200. The scalar dissipation rate field (computed as $\nabla\zeta\cdot\nabla\zeta$ using the conserved scalar field shown in Figure 3a) is shown in Figure 3b. In this

figure, the lowest dissipation regions are colored black, and the remaining 255 gray levels correspond to linearly increasing dissipation. Figure 3e shows a contour plot of the principal compressive strain normalized by the outer scale strain. A comparison of Figure 3b and Figure 3e shows that the size of the strain structure is of the same order as the dissipation layer structure, an observation that is consistent with what is expected for $Sc \approx 1$ mixing. Regions of high dissipation and high strain rate are correlated fairly well, as shown in Figure 3f. In this figure, a contour plot of the dissipation rate field has been overlaid with a plot of the principal strain vectors. It can also be seen that the principal strain directions line up with the layer normal directions fairly well, a result that is dealt with quantitatively later.

Figure 4 shows the strain and dissipation profiles for some layers taken from the dissipation image shown in Figure 3b. In this figure, both the dissipation and the strain have been normalized by the respective maximum values along the layer. It is seen that dissipation layers exhibit a Gaussian shape in a majority of the cases, whereas the strain profiles are more complex, and they do not exhibit any characteristic shapes. It is also found that overlap of peaks in the strain and dissipation fields is not very common. In most of the cases, the strain reaches a maximum along the layer at a point different from the point where the dissipation reaches a peak. Figure 5 shows the distribution of the principal compressive strain, normalized by the inner scale strain, $S_{is} = (\Delta U_c/\delta_{50\%})(Re_{\delta 50\%})^{1/2}$. It is found that the most probable value of the strain is around a tenth of the inner scale strain.

Since there is a significant variation of strain along the layers, the choice of a suitable strain in the computation of α (Equation 5) becomes an issue. Since the dissipation layer was defined based on the 20% point, we define an average strain, which is equal to the average strain across the 20% dissipation points in the layer. This value is used in the computation of the scaling parameter, α. The resulting distribution of the parameter α, computed for hundreds of layers and at several Reynolds numbers, is shown in Figure 6. The horizontal axis in the plot is the principal compressive strain rate divided by the inner scale strain. The layer thickness used in the computation of α is the full width at the 20% points of the dissipation profile. The 1-D, steady theory (Equation 5) predicts that all dissipation layers should have the universal value of α=0.4 (also shown on Figure 6). The figure shows that for the lower valued strains, α is greater than 0.4, or the measured layers are *thinner* than the steady state value. On the other hand, for higher strains, $\alpha < 0.4$ or the layers are *thicker* than the steady state value. It is also noted that these trends are essentially similar for all of the Reynolds numbers considered.

These results suggest that in unity Schmidt number turbulent flows, it may not be possible to predict the layer thickness correctly by modeling the dissipation field as simply an ensemble of 1-D, steady, strained, laminar diffusion layers. As Figure 6 shows, the measured layers rarely follow the theoretical scaling law. There are many possible reasons for this disagreement. One limitation is that only 2-D data are available, which means that that the computed principal strain would be in error in regions where the measurement plane is not orthogonal to the layer. By selecting only high dissipation layers, we expect to minimize this effect, but three-dimensionality cannot be ruled out as a cause for the observed trend.

Furthermore, the strain and dissipation profiles in Figure 4 show that the strain is not uniform across the layer, whereas in the theory we assumed constant strain across the layers. However, we investigated the effect of non-uniform strain using a numerical solution of the 1-D steady scalar transport equation, in which the strain was assumed to have a Gaussian profile across the layer. We concluded that in cases where the width of strain profile was at least as large as the scalar dissipation layer, then the non-uniform strain had little effect on the structure of the dissipation layer (provided the mean strain over the layer was the same). Still another question is whether we are measuring relatively thick dissipation layers because the compressive strain is not aligned orthogonal to the layer. If this were the case, the strain used should be the component of strain that is orthogonal to the layer. The degree of misalignment, θ, which is defined as the angle between the direction of the most compressive strain and the layer normal, is shown in Figure 7a. This angle was found for all the layers, and a histogram is plotted in Figure 7b. The figure shows that there is very good alignment between the strain and dissipation normal direction. This means that using the component of strain orthogonal to the layer will have only a marginal effect on the results shown in Figure 6.

Although we believe that the measurements have sufficient spatial resolution, the data of Fig. 6 are consistent with what would be expected from finite resolution, i.e. that the layers tend to be too large. However, if this were the case, then we would expect better agreement at the lower Reynolds numbers and the

lower levels of strain as the layer thickness measurement would be better resolved. However, for low strains, Figure 6 shows that there is not an improvement in agreement with the theoretical value. In fact, at very low strain rates, the layers are actually too small. It appears then, that resolution effects alone cannot fully explain the trend seen in Figure 6.

The most likely reason for the difference between the simple theory and experiment is the effect of unsteadiness. In other words, once the strain is applied, perhaps the dissipation layers do not have time to establish the steady state structure before the strain changes. The analytical solution to the unsteady equation shows that the variation of dissipation layer thickness with time is given by[6]

$$\lambda_D = \exp\left(-\int_0^t 2S_{xx}(t')dt'\right)\left[\lambda_D^0 + 2\nu\int_0^t \exp\int_0^{t'} 2S_{xx}(t'')dt''dt'\right]$$

According to this equation, the time taken to reach steady state is determined by the leading decaying exponential term, and is of the order of the inverse of the final strain. However, this time-to-steady-state is of the same order as the characteristic time of the strain rate field in a turbulent flow. In this case, it might be expected that the dissipation structures will indeed not have time to achieve their steady state values. It is for this reason that we investigated unsteady strain effects with a numerical solution of the unsteady scalar transport equation with an imposed oscillating strain field. This analysis is dealt with in detail in the next section.

Effect of oscillating strain on dissipation layer structure

The governing equation (Equation 1) was solved assuming an imposed sinusoidally varying strain rate field. The instantaneous strain rate field, S_{xx} was given by

$$S_{xx}(t) = S_{xx}^{mean} + \Delta S_{xx}\sin(\omega t)$$

where ω is the frequency of oscillation, and $\overline{S}_{xx}$ is the mean strain rate. For the sake of simplicity, the assumption that the strain rate is uniform in space is retained.

Equation 1 was then solved numerically at each time step using a second order implicit scheme. The boundary conditions for this problem are that the scalar concentration gradient is zero far away from the layer. The steady state solution was used as the initial condition, upon which the oscillation was subsequently imposed.

In order to relate better to the experimental results, the amplitude and frequency of oscillation were chosen so that the resulting strain varied over the same range of values as that measured in the experiment. It is emphasized that no attempt was made to simulate the actual strain field, but only to draw some qualitative conclusions about the effect of unsteadiness. The strain was chosen to vary from 100 to 1200 sec^{-1} (corresponding to S_{xx}^{mean} =650 sec^{-1} and ΔS_{xx} =1100 sec^{-1}) with varying frequencies of oscillation ranging from the mean strain rate to a hundredth of the mean strain rate.

Figure 8 shows the imposed strain rate field, the theoretical steady-state layer thickness, and the computed layer thickness as a function of time. The theoretical steady state layer thickness was computed from Equation 6 using the instantaneous value of S_{xx}. The frequency of oscillation of the strain field in this case was the same as the mean strain rate. Based on the understanding that the time to steady state of the dissipation layers is of the order of the inverse of the strain, we would expect the computed layer thickness to be close to the steady state value for the higher valued strains. Figure 8 shows that the computed layer thickness is close to, but larger than, the steady state value for the high valued strains. The figure also shows that for the low valued strains, the steady state assumption grossly overpredicts the layer thickness, since the computed layer thickness are approximately three times smaller for the lowest valued strain. Figure 8 also shows that the computed unsteady thickness waveform exhibits a phase shift with respect to the strain waveform. In other words, for a steady state system, we expect the layer thickness to be a minimum when the strain is a maximum. This is clearly not the case, as is expected for a system with a finite response time.

When the frequency of oscillation is low, we would expect that the dissipation layers would have enough time to reach the steady state, in which case the computed layer thickness would be expected to be close to the steady state thickness for a wide range of strains. Figure 9 shows the instantaneous strain rate, steady state layer thickness and the computed layer thickness

corresponding to a frequency equal to a hundredth of the mean strain. The figure shows that the computed layer thickness does follow the steady state value closely, though it still does not agree at the lowest valued strains. This is to be expected, since the steady state structure is established much faster for high strains.

This effect of the magnitude of the imposed strain is seen in Figure 11, which shows α plotted as a function of time for two values of the final strain. The first corresponds to a step increase in strain (500 sec^{-1} to 1500 sec^{-1}) and the second to a step decrease in strain (500 sec^{-1} to 100 sec^{-1}). The parameter, α, is evaluated for each case using the final strain value. When the strain increases from 500 sec^{-1} to 1500 sec^{-1}, the dissipation length scale is strain limited and the dissipation layer quickly reaches the steady state, which occurs within a time of about 0.002 sec. On the other hand, when the imposed strain field is changed from 500 sec^{-1} to 100 sec^{-1}, the dissipation length scale is diffusion dominated and it takes much longer (about 0.02 sec) for the layer to reach its steady state. Thus at lower strains, the dissipation field takes much longer to reach a steady state.

In order to relate these results to the experimental results, the 20% dissipation layer thickness was found, and values of the non-dimensional parameter α computed. Figure 10 shows the parameter α plotted as a function of the instantaneous strain for two different frequencies of oscillation. For the low frequency case, the layers are at a quasi-steady state, and the value of α is very close to the steady state value of 0.4 for almost all values of strain. When the frequency of oscillation is of the order of the mean strain rate, the resulting layers are always *thinner* than the corresponding steady state value for low strains, and this explains the very high values of α obtained at low strains, as shown in Figure 11. For the higher strains, the value of α falls below 0.4, since the layers are now slightly thicker than the steady state value (as was seen in Figure 9). A comparison of Figs. 6 and 11 shows that the unsteady strain numerical solution at least captures the qualitative trends observed in the measured data. We note however, that since no attempt was made to simulate the actual strain fields in the flow, only this qualitative comparison is possible at this time.

Conclusions

Simultaneous PIV/PLIF data were used to perform a study of the dissipative length scales in a near unity Schmidt number turbulent planar jet flow. The alignment of the principal strain rate is found to be orthogonal to the dissipation layer normal in most of the cases, which is consistent with what has been reported by previous experimental and numerical studies. The magnitude of measured strain is consistent with what is expected from classical turbulence theory. However, the measured layer thicknesses do not follow the theoretical scaling based on uniform, steady strain. The results indicate that it is not possible to model the dissipation layers as an ensemble of 1-D steady, strained laminar diffusion layers. A numerical study of the unsteady scalar transport equation shows that the dissipative layer length scales do not respond fast enough to a change in the strain, and trends seen in the unsteady simulation are similar to those seen in experiment. Based on these results, it is concluded that accurate prediction of dissipative layer structure in such flows is possible only if the unsteadiness in the strain field is taken into account.

References

1. N. Peters (1984), "Laminar diffusion flamelet models in non-premixed turbulent combustion," *Prog. Energy Combust. Sci.*, **10**, pp. 319-339.

2. R. W. Bilger (1976) *Comb. Sci. Tech.*, **13**, pp. 155-170.

3. Su, L.K. and Dahm, W.J.A. (1996) "Scalar imaging velocimetry measurements of the velocity gradient tensor field in turbulent flows. II. Experimental results". *Phys. Fluids* **8**, pp. 1883-1906.

4. R.M. Kerr (1985) "Higher order derivative correlations and the alignment of small scale structures in isotropic numerical turbulence." *J.Fluid Mech.* Vol. 153, pp31-58

5. W.T. Ashurst, A.R. Kerstein, R.M. Kerr, and C.H.Gibson (1987) "Alignment of vorticity and scalar gradient with strain rate in simulated Navier Stokes turbulence" *Phys. Fluids* **30**, pp. 2343-2353.

6. K.A. Buch, Jr. and W.J.A. Dahm (1996) "Experimental study of the fine scale structure of conserved scalar mixing in turbulent shear flows. Part 1. Sc » 1." *J.Fluid Mech* **317**, pp. 21-71.

7. J.E. Rehm (1999) "The effects of heat release on turbulent nonpremixed planar jet flames" Ph.D. Dissertation, Dept. of Aerospace Engineering and

Engineering Mechanics, The University of Texas at Austin.

8. J.E.Rehm (1999) “The association of scalar dissipation rate layers and OH zones with strain, vorticity, and 2-D dilatation fields in turbulent nonpremixed jets and jet flames” **AIAA-99-0676,** January 1999.

9. J. E. Rehm and N. T. Clemens (1998) "The Relationship between Vorticity/Strain and Reaction Zone Structure in Turbulent Non-Premixed Jet Flames" Twenty Seventh Symposium on Combustion, pp. 1113-1120.

10. J.E. Rehm, N.T. Clemens (1999) “An improved method for enhancing the resolution of conventional double-exposure single-frame particle image velocimetry” *Exp.Fluids,* **26** pp 497-504.

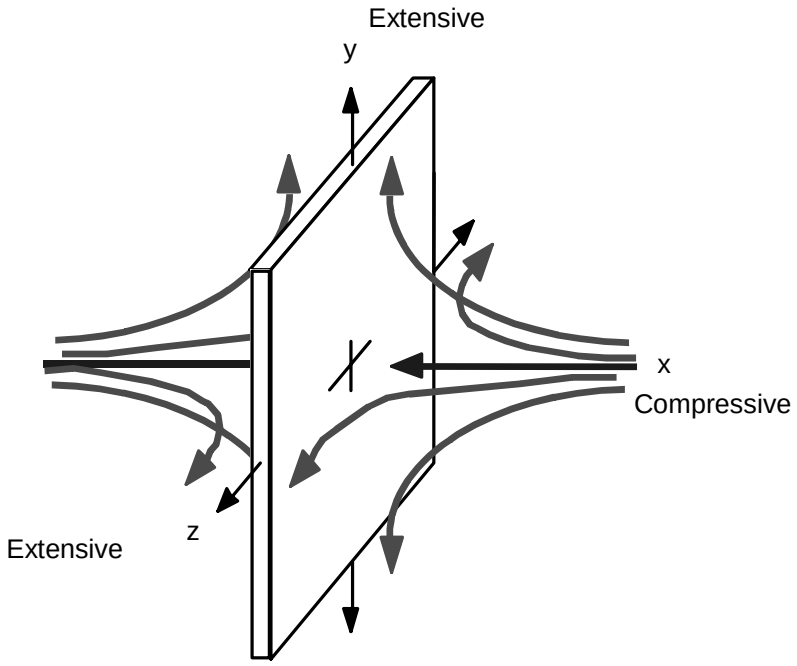

Figure 1: Illustration of a scalar dissipation layer produced by a sheet-forming strain field.

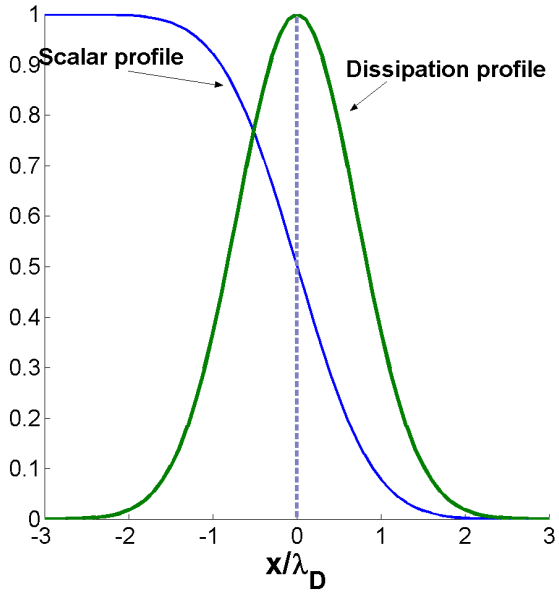

Figure 2: Theoretical profiles of scalar concentration and dissipation across the layer.

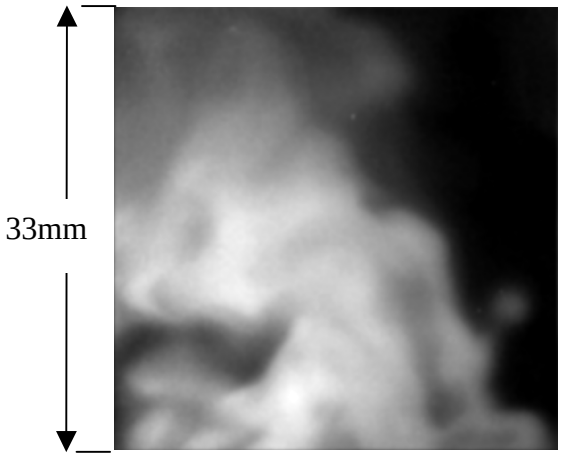

(a) Sample PLIF image

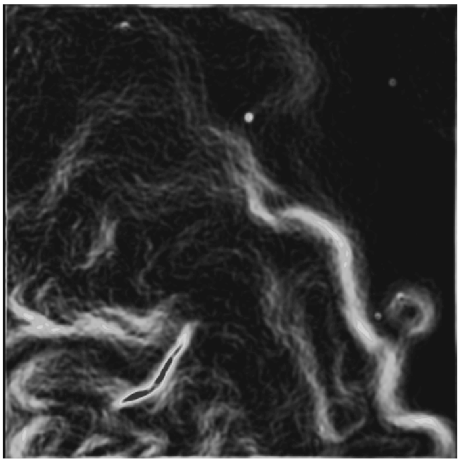

(b) Scalar dissipation image

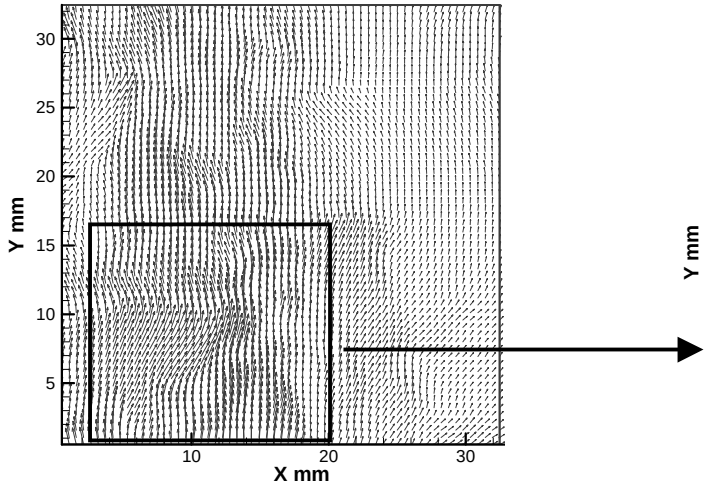

(c) PIV vector field, 32×32 window

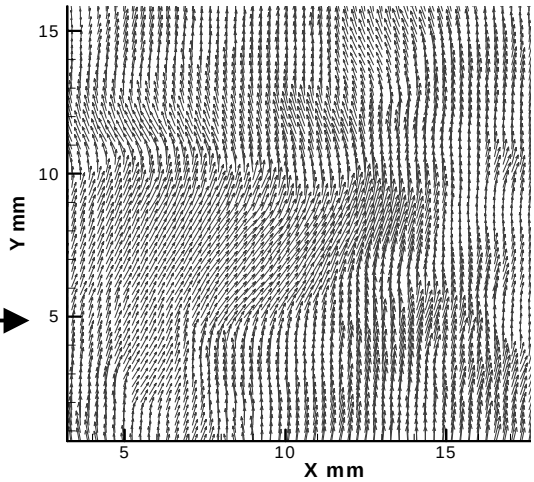

(d) PIV/PTV vector field in the boxed region shown on left

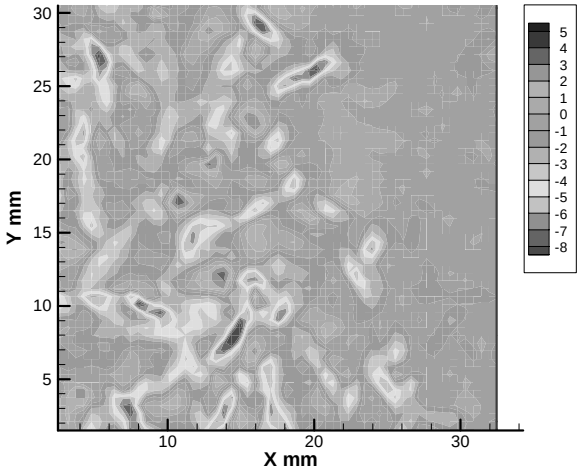

(e) Contours of 2-D principal compressive strain

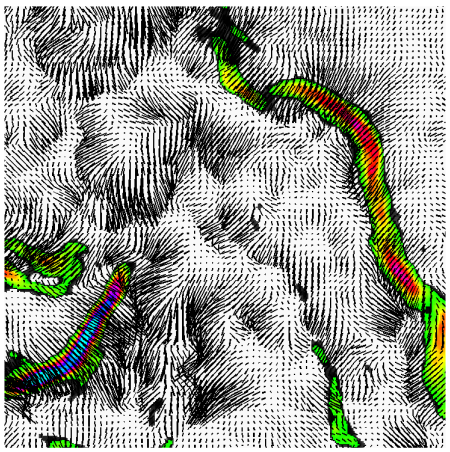

(f) Principal strain directions superimposed on dissipation field

Figure 3: Sample data, Re_δ= 4200

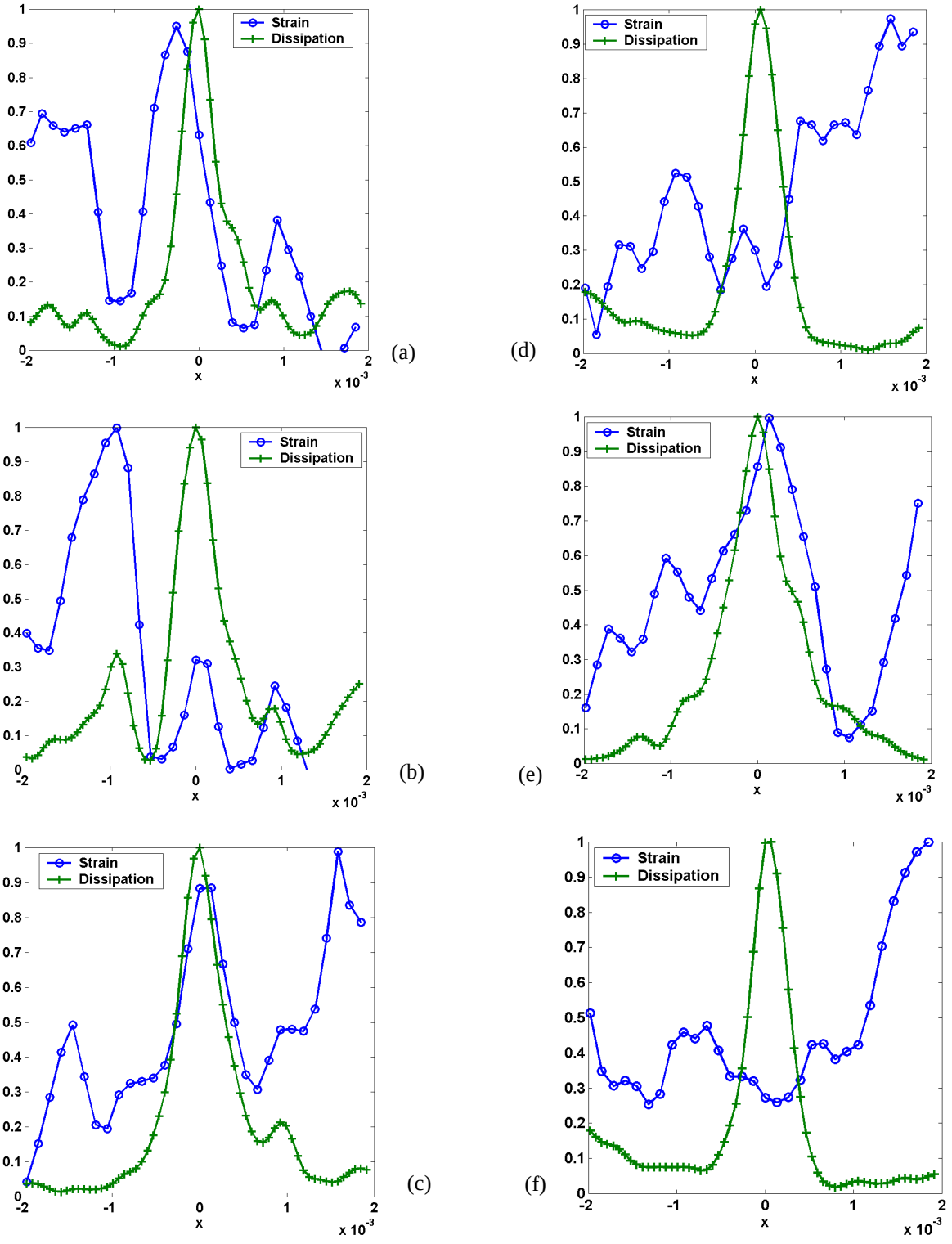

Figure 4: Sample profiles of measured strain rate and scalar dissipation across the layers.

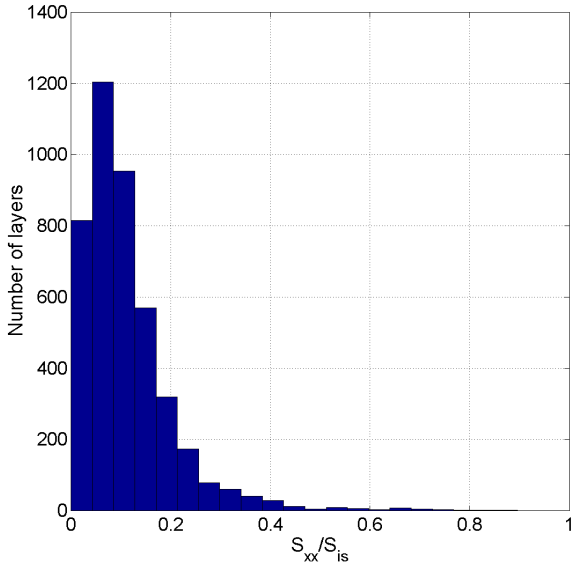

Figure 5: Distribution of the measured strain rate normalized by the inner-scale strain.

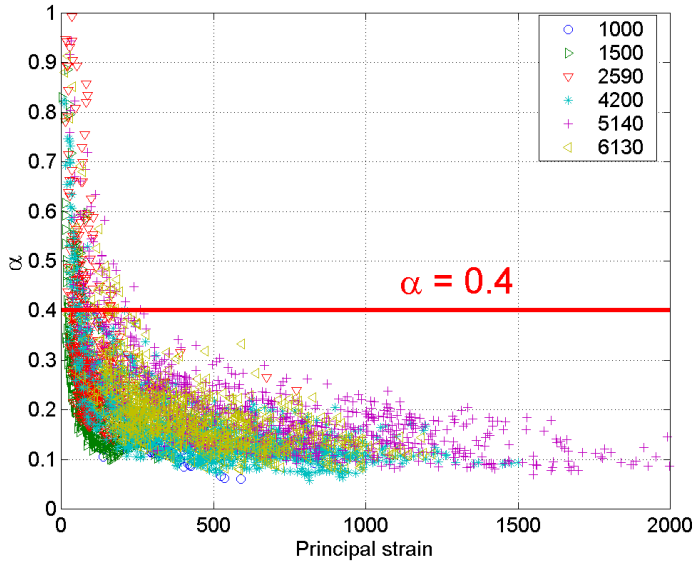

Figure 6: Scaling parameter as a function of strain.

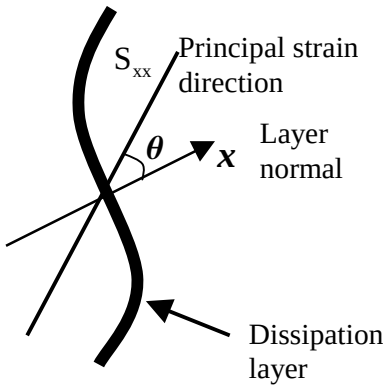

Figure 7a: Definition of the direction of the principal strain and dissipation layer normal direction.

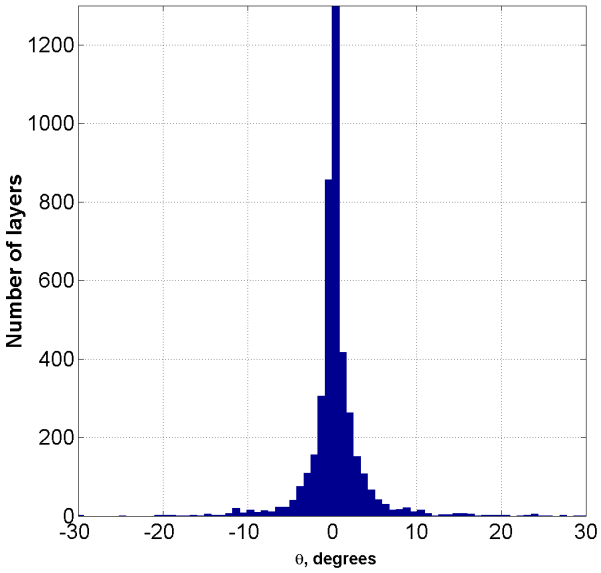

Figure 7b: Histogram of the angle θ measured for several layers.

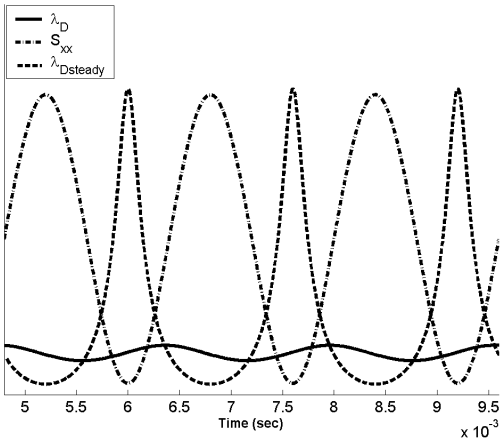

Figure 8: Effect of oscillating strain, Frequency = S_{xx}^{mean}.

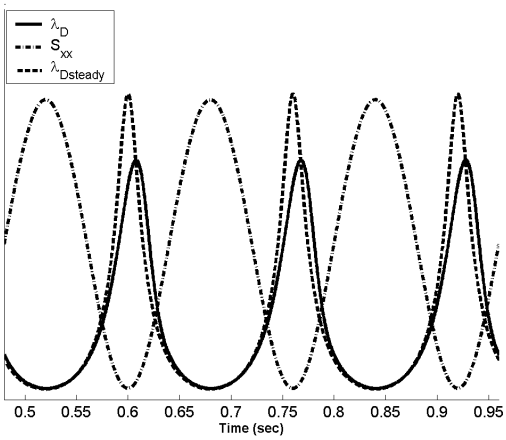

Figure 9: Effect of oscillating strain, Frequency = 0.01 S_{xx}^{mean}.

$$\alpha = \frac{1}{\lambda_D}\sqrt{\frac{D}{S_{xx}}}$$

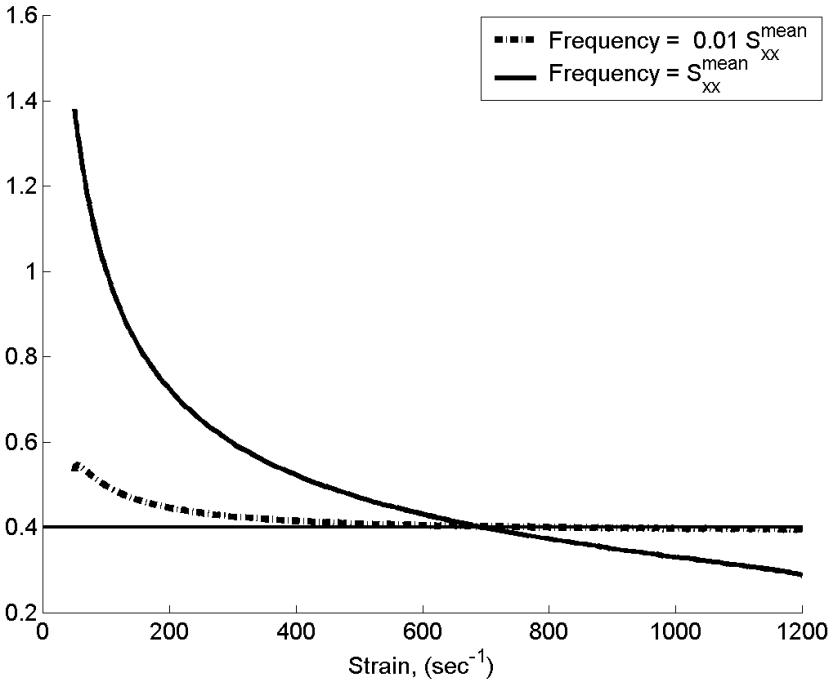

Figure 10: Distribution of α versus strain compiled from the computed data shown in Figs. 8 and 9.

$$\alpha = \frac{1}{\lambda_D}\sqrt{\frac{D}{S_{xx}}}$$

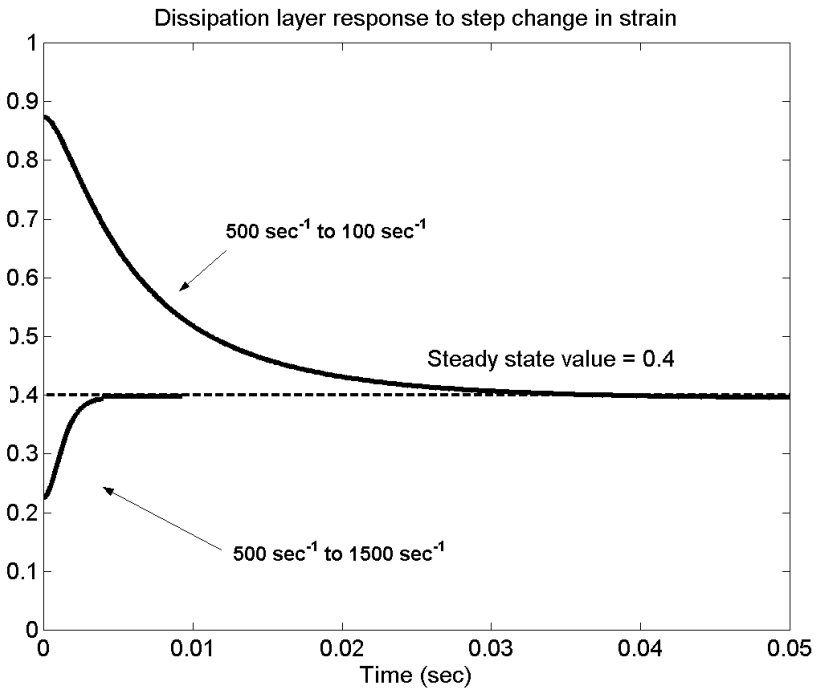

Figure 11: Dissipation layer response to step change in strain.